Volume 1 | Number 1 | Jan 2013 | Pages 1–100

Journal of
Materials Chemistry A

Materials for energy and sustainability
www.rsc.org/materialsA

Li⁺

ROYAL SOCIETY
OF CHEMISTRY

ROYAL SOCIETY
OF CHEMISTRY

www.rsc.org/materialsA

Effects of structural disorder and nitrogen content on oxygen reduction activity of polyvinylpyrrolidone-derived multi-doped carbon

Raghunandan Sharma[a], Kamal K. Kar [b,*]

Multi-doped carbons, with high N-content (~11 wt.%, bulk) and presence of C- and N- bound O/Co were synthesized by pyrolysis of polyvinylpyrrolidone (PVP) and cobalt nitrate ($Co(NO_3)_2.6H_2O$) mixture at various temperatures (T_p) ranging from 400 to 800 ^{o}C. To study the effects of surface modification on the oxygen reduction reaction (ORR) activity, doped carbon (CN_x) samples were further acid-treated with nitric acid (HNO_3). Structural characterizations by Raman spectroscopy and X-ray diffraction reveal an amorphous phase of carbon for T_p of 400 to 700 ^{o}C, and a partially graphitic structure for T_p of 800 ^{o}C. Electrocatalytic performance of as-synthesized and acid-treated CN_x determined by linear sweep as well as cyclic voltammetry in 0.1 mol L^{-1} KOH electrolyte reveal significant catalytic activities with an ORR onset potential of -144 mV (vs Ag/AgCl), as compared to -210 mV of Pt electrode under similar conditions. Correlations between the electrochemical parameters and the structural parameters such as degree of disorder and N-content suggest high electrocatalytic activity for CN_x with low disorder and high N-content. In addition to high ORR activity, the CN_x samples synthesized at lower T_p also exhibit catalytic activity for methanol oxidation, which makes them suitable catalyst support for direct methanol fuel cells.

INTRODUCTION

Oxygen reduction reaction (ORR), a sluggish yet important reaction in the electrochemical energy conversion devices (alkaline fuel cells, polymer electrolyte membrane fuel cells, etc.), is conventionally catalyzed by Pt-nanoparticles supported on high surface area carbon materials. Despite their best till-date performance in terms of catalytic activity and stability, Pt-based ORR-catalysts are still inappropriate in large-scale applications due to the high cost, scarcity and carbon monoxide poisoning of Pt. Considerable efforts aiming to develop a cost effective substitute of the Pt-based ORR-catalysts are being made during the last few decades.

Since the first demonstration of the electrocatalytic activity of transition metal doped porphyrins and phthalocyanines by Jasinski,[1] various metal-free and non-precious metal (NPM)-based catalysts such as N-doped[2, 3] and S- and N-codoped[4, 5] porous carbons, N doped carbon nanotubes (CNTs)[6, 7], graphene (N-doped graphene[8-13], B-doped graphene[9], B-and N-codoped graphene[9, 14], S- and N-codoped graphene[15]), and NPM-based catalysts derived from transition metal–macrocycles, electroconductive polymers,[16-20] etc. have been demonstrated as the Pt-free ORR electrocatalysts. Catalytic activity of the metal-free catalysts stems from the presence of heteroatoms in the carbon network, which form the ORR active sites by imparting positive charge on the surrounding carbon atoms.[6, 21] Although the true nature of the catalytically active sites in doped carbon (CN_x) electrocatalysts is debatable, various carbon-heteroatom bonding configurations are considered to be responsible for the catalytic activity.[22] Therefore, the electrocatalytic performance of CN_x may be altered by varying the density of such active sites either by increasing the dopant concentration[23] or by altering other structural parameters such as chemical state, degree of disorder (α_D) and surface structure[24] of CN_x. For example, in N-doped carbon, since the pyridinic-N sites are located at the edges of graphitic planes, their density is governed by the extent of edge plane exposure.[22, 25, 26] Hence, by decreasing crystalline size, the edge plane exposure can be increased to attain higher number of disordered (pyridinic-N or pyrrolic-N) sites.

Structure of catalytically active sites and dopant concentration of the CN_x electrocatalysts are influenced largely by the synthesis conditions and the precursors used. [23, 27] Numerous N-containing

[a]Advanced Nanoengineering Materials Laboratory, Materials Science Programme
Indian Institute of Technology Kanpur, Kanpur-208016, India, Email: raghumsp@iitk.ac.in, sharmariitk@gmail.com, Ph. # 0512-2597818
[b]Advanced Nanoengineering Materials Laboratory, Materials Science Programme, and Department of Mechanical Engineering, Indian Institute of Technology Kanpur, Kanpur-208016, India, Email: kamalk@iitk.ac.in, Fax # 0512-2597408, Phone # 0512-2597687
Corresponding author. Fax: +91 512 2597408; E-mail address: kamalk@iitk.ac.in (Kamal K. Kar).

precursors including aliphatic (acetonitrile,[22] ethylenediamine,[2] etc.) and heterocyclic aromatic (pyridine,[20] melamine,[28] etc.) compounds, polymers (polyaniline,[29, 30] polypyrrole,[31] etc.), materials obtained from biomass (soybean,[3] silk,[32] etc.) and others have been used to synthesize metal-free or NPM based electrocatalysts. However, the effects of processing parameters such as temperature, surface modifications, etc. on the structural parameters such as crystallinity and number of ORR active sites, and their subsequent effects on the electrocatalytic activity of CN_x have not been studied extensively.

Similar to the metal-free CN_x, NPM based catalysts have metal-carbon bonding as catalytically active sites.[33, 34] However, despite significant efforts, the NPM-based catalysts lack of stability and activity required to be suitable for the ORR-catalysis. More recently, NPM-based catalysts with high ORR performance and stability have been prepared by co-doping of metallic as well as nonmetallic heteroatoms in the carbon matrix. Among various metal/nonmetal codoped carbons, Co and N doped ones have shown superior performance in terms of both ORR activity and stability.[19, 27, 33, 34]

The enhancement of catalytic activity of Pt-free catalysts can also be attained by using nanocomposites of various carbon nanomaterials and/or NPM-based oxides, alloys, etc., where various steps of the reaction may be catalyzed by different phases of the nanocomposite catalyst. Recently, Liu et al. have shown high photocatalytic activity of metal free, carbon nanodot–carbon nitride nanocomposite photocatalyst for water-splitting, where two steps of the overall reaction, namely photocatalysts and chemical catalysis were performed respectively by carbon nitride and carbon nanodots.[35]

In the present study, we demonstrate the fabrication of an N-, O- and Co-codoped carbon electrocatalyst for ORR catalysis. The effects of processing parameters on the structure and the ORR performance of CN_x synthesized by low to medium temperature (400 to 800 ^{o}C) pyrolysis of polyvinylpyrrolidone (PVP), a novel, N- and O- containing polymeric precursor were studied. The low temperature synthesis of CN_x having high N- and O- contents was made possible by the use of PVP as precursor since it carbonizes at a pyrolysis temperature (T_p) of < 450 ^{o}C. Apart from this, other obvious advantages of PVP included its (i) water

solubility, which offers easy mixing with transition metal salts; (ii) cost-effectiveness compared to other polymeric precursors; and (iii) non-toxic nature. In this study, the effects of pyrolysis temperature and surface treatment on the structure of CN_x were determined respectively by using a set of T_p to synthesize CN_x and by subjecting the as-synthesized CN_x to an acid treatment. The parameters α_D and X_N, associated respectively to the nature and number of active sites, were considered as the structural parameters of interest. Finally, the effect of structural evolution on the ORR performance was studied by correlating the ORR performance parameters with the structural parameters.

EXPERIMENTAL

Synthesis of CN_x

CN_x were synthesized by one-step pyrolysis of an homogeneous mixture of PVP (1.389 g) and $Co(NO_3)_2.6H_2O$ (0.494 g), prepared by mixing the materials in deionized water (10 ml) with magnetic stirring for 2 h followed by drying at 100 ^{o}C for ~10 h. The amounts of PVP and $Co(NO_3)_2.6H_2O$ were selected to obtain a Co/C weight ratio of 0.1 for the mixture. The pyrolysis was performed in a horizontal quartz tube furnace pursed with a continuous flow of N_2 (200 ml min^{-1}). The reactor temperature was increased to the desired value with a heating rate of 3 ^{o}C min^{-1} and held for 30 min to complete the pyrolysis process. To study the effects of T_p on the electrocatalytic activity, five different T_p values of 400, 500, 600, 700 and 800 ^{o}C were selected to synthesize the catalysts $CN_x/400$, $CN_x/500$, $CN_x/600$, $CN_x/700$ and $CN_x/800$, respectively. Finally, to remove the Co-oxide/Co particles and part of disordered carbon from the sample and to modify the surface morphology, the as-synthesized samples were treated with 5M HNO_3 for 24 h followed by washing and filtering severally with deionized water till neutral pH to obtain the acid-treated CN_x (A/CN_x) samples, namely A/CN_x/400, A/CN_x/500, A/CN_x/600, A/CN_x/700 and A/CN_x/800 corresponding to the T_p of 400, 500, 600, 700 and 800 ^{o}C, respectively.

Structural characterizations

2 | *J. Mater. Chem. A*, 2015, **00**, 1-16

This journal is © The Royal Society of Chemistry 20xx

Thermal degradation of PVP and PVP/Co(NO$_3$)$_2$.6H$_2$O mixture (Co-PVP) were studied by thermogravimetric analysis (TGA) using a Perkin-Elmer Diamond TG/DTA analyzer. To study the surface morphologies of the electrocatalysts, scanning electron microscope (SEM) and atomic force microscope (AFM) imaging were performed using a Zeiss, EVO MA-15 SEM and an Agilent 5500 AFM, respectively. Again, the elemental composition was determined by using a carbon-hydrogen-nitrogen (CHN) analyzer (PerkinElmer Series-II CHNS/O Analyzer 2400) and an energy dispersive X-ray (EDX) analyzer (Quanta 200 SEM). Raman spectra were recorded on a Horiba Jobin Yvon LabRAM HR Raman microscope using a laser excitation source of 632.7 nm to evaluate α_D of the CN$_x$ electrocatalysts. Analysis of Raman spectrum was performed by fitting the data with a Voigt distribution function, consisting of a combination of Gaussian and Lorentzian components. To study the effects of processing parameters such as T$_p$ and acid-treatment on the crystalline order, X-ray diffraction (XRD) patterns of as-synthesized and acid-treated CN$_x$ were obtained by using Rigaku Miniflex 600 X-ray diffractometer with Cu Kα (λ = 1.5418 Å) radiation at a scan rate of 0.5^o min^{-1}. Finally, Fourier transform infrared (FTIR) spectroscopy (Bruker Vertex-70) and X-ray photoelectron spectroscopy (XPS; PHI 5000, Versa Prob II, FEI Inc. spectrometer) were employed to probe the chemical state of the CN$_x$ electrocatalysts. Finally, cyclic voltammetry (CV) was performed using an electrochemical cell attached with an Agilent 5500 AFM, while linear sweep voltammetry (LSV) was performed on a homemade rotating-disk-electrodes (RDE) setup.[36]

Electrode preparation and electrochemical characterizations

A three-electrode setup quipped with a modified glassy carbon (GC) working electrode, an Ag/AgCl (1.0 M KCl) reference electrode and a Pt-wire counter electrode was used for the CV measurements. The GC electrodes (disc diameter: 3 mm) were cleaned carefully by acid-treatment, polishing and ultrasonication. After dipping in 10% (v/v) HNO$_3$ for 10 min, GC electrodes were washed with deionized water and polished with 0.3 μm alumina powder. Finally, the electrodes were ultrasonicated successively in deionized water and ethanol (5 min, each). Dispersions of the catalysts were prepared by mixing each of the powdered samples in ethanol (1 g L^{-1}) by ultrasonication for 60 min. To prepare a working electrode, 25 μl of the catalyst

dispersion was drop-casted on a cleaned GC electrode and air-dried for at least 60 min. Finally, 2.5 μl of 1.0 wt.% polystyrene solution in xylene was drop-casted and air-dried on the CN$_x$ modified electrode, which worked as the binder during the CV measurements. For a particular catalyst, three similar working electrodes were prepared.

CV measurements were carried out in a potential range of -1.0 to 0.2 V at a scan rate of 50 mV s^{-1} in O$_2$-saturated as well as Ar-saturated 0.1M KOH electrolytes. Furthermore, LSV measurements on CN$_x$ modified GC RDE were carried out in similar electrolytes at a potential scan rate of 10 mV s^{-1} and a rotation rate of 1600 rpm. To remove the capacitive current, the LSV curves obtained in presence of Ar were subtracted from the corresponding ones obtained in O$_2$ saturated electrolytes. Similarly, for evaluation of the methanol oxidation reaction (MOR) activity, CV measurements were performed in an electrolyte containing 1.0 mol L^{-1} H$_2$SO$_4$ and 1.0 mol L^{-1} CH$_3$OH at a scan rate of 50 mV s^{-1}. Finally, the ORR activities of the CN$_x$ electrocatalysts were compared in terms of various parameters extracted from the CV curves and the RDE voltammograms.[37]

RESULTS AND DISCUSSIONS

Thermal degradation of PVP

TGA and temperature derivative of weight (dW/dT) curves of Fig. 1 reveal the thermal degradation of pure PVP and Co-PVP in N$_2$ environment. The thermal degradation of Co(NO$_3$)$_2$.6H$_2$O has been reported to take place in a temperature range between 160 and 260 ^{o}C with a weight loss of ~ 72% according to the scheme-

$$2Co(NO_3)_2.6H_2O \xrightarrow{-37\ wt.\%} 2Co(NO_3)_2 \xrightarrow{-34\ wt.\%} Co\ Oxides$$

to form cobalt oxides (Co$_3$O$_4$, Co$_2$O$_3$ and CoO). [38][39] A comparison between the TGA curves for PVP and Co-PVP suggests an additional weight loss for the latter in a temperature range between 170 to 360 ^{o}C (marked by A), corresponding to decomposition of Co(NO$_3$)$_2$.6H$_2$O. Again, while the thermal degradation of pure PVP completes below 450 ^{o}C, the Co-PVP decomposes over a broader temperature range with a residual weight of ~20 % at 800 ^{o}C, which, after compensating for the difference due to the presence of Co$_3$O$_4$ (7.4 %), is ~10 % higher than that of the latter. The higher residual weight and broader range of weight loss are attributed to the modified thermal

This journal is © The Royal Society of Chemistry 20xx

J. Mater. Chem. A, 2015, **00**, 1-16 | **3**

decomposition of PVP in presence of the metal salt. As the onset points of PVP carbonization (marked by arrows) lie below 400 °C, a set of temperatures ranging from 400 to 800 °C was selected for the present study.
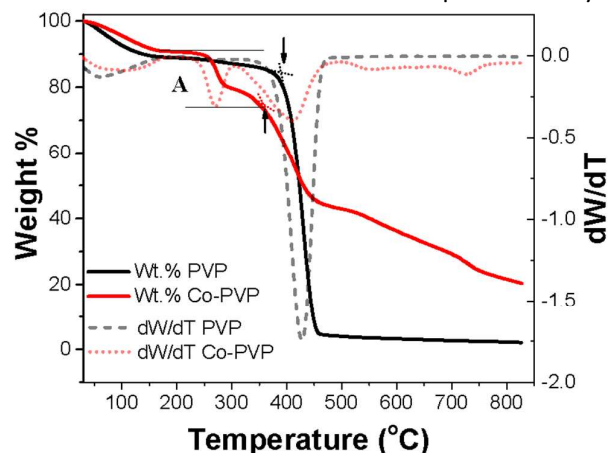

Fig. 1: TGA and derivative weight (dW/dT) curves of the PVP and PVP/Co(NO$_3$)$_2$.6H$_2$O mixture obtained at a scan rate of 10 °C min^{-1} in N$_2$ environment.

Structural characterizations

XRD patterns of the as-synthesized as well as acid-treated CN$_x$ are shown in Fig. 2, which exhibit no diffraction peaks corresponding to graphite for the CN$_x$ or the A/CN$_x$ synthesized below 800 °C, unveiling their amorphous nature. For T$_p$ below 800 °C, appearance of a broad peak around 2θ of 25° on acid treatment may be attributed to the increased short-range order by removal of highly disordered carbon from the catalyst. For CN$_x$/800, appearance of diffraction peaks corresponding to the (002), (100), (101) and (004) planes of graphite (JCPDS 41-1487), reveals the presence of partially crystalline graphitic phase. This is attributed to the catalytic effect of Co, leading to graphitization during pyrolysis.[40] Again, both untreated as well as acid-treated CNx samples synthesized at 800 °C exhibit similar graphitic nature except the increased intensity of graphitic peaks with acid-treatment. This may be attributed to the removal of amorphous carbon during acid-treatment. Pyrolysis of Co-PVP at 400 °C forms a nanocomposite consisting of cobalt oxides embedded in the N- and O-containing amorphous carbon matrix. Diffraction peaks corresponding to three different types of cobalt oxides, namely CoO (2θ ~ 36, 42; JCPDS- 78-0431), Co$_2$O$_3$ (2θ ~ 26, 31, 38, 51; JCPDS-02-0770) and Co$_3$O$_4$ (2θ ~ 31, 37, 45, 56; JCPDS- 78-1969) are observed in CN$_x$-400. At T$_p$ value of 500 °C, the peaks corresponding to Co$_3$O$_4$ and Co$_2$O$_3$ disappear and the samples consist of CoO in amorphous carbon, while metallic Co (2θ ~44, 51; JCPDS- 15-0806) phase appears along with CoO at T$_p$ of 600 °C. Again, at higher T$_p$ (700 and 800 °C) the CoO phase disappears completely while the metallic Co phase prevails in the graphitic carbon matrix. The formation of metallic Co at higher T$_p$ attributes possibly to the reduction of CoO by the by-products (hydrocarbons, hydrogen) of PVP pyrolysis. Furthermore, XRD patterns of A/CN$_x$ (Fig. 2b) exhibit no peaks corresponding to Co-oxides suggesting their complete removal during the acid treatment. On the other hand, the metallic Co phase for CNx synthesized at T$_p$ values of 600-800 °C is not removed completely on acid-treatment.
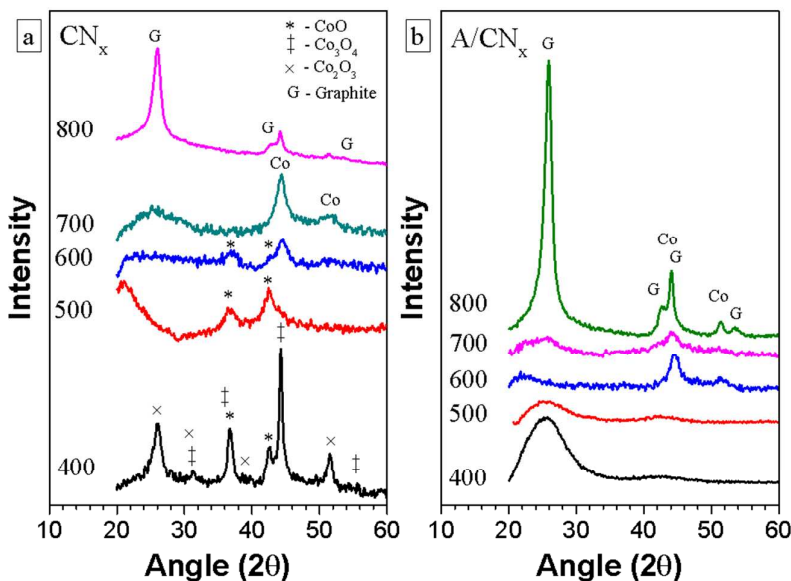

Fig. 2: X-ray diffraction (XRD) patterns of (a) CN$_x$ and (b) A/CN$_x$.

4 | *J. Mater. Chem. A*, 2015, **00**, 1-16

This journal is © The Royal Society of Chemistry 20xx

Raman spectra of CN_x and A/CN_x synthesized at varying T_p values are shown in Figs. 3a and 3b. The CN_x synthesized at lower temperatures (400-500 ^{o}C) exhibit the overlapped D (~1365 to ~1329 cm^{-1}) and G (~1585 cm^{-1}) bands, revealing their amorphous/disordered nature and presence of C-N defects.[41] With increasing T_p, the overlapped D and G bands are resolved, which is attributed to the increased graphitic order. In addition to the graphitic D and G bands, a weak D'-band at ~ 1615 cm^{-1} is also observed for CN_x synthesized at T_p of 800 ^{o}C, suggesting a relatively lower disorder.[42] This is consistent with the XRD analysis, which suggests the appearance of graphitic structure for CN_x/800 and A/CN_x/800. Again, no significant shift in the G-band positions for both CN_x as well as A/CN_x are observed with increasing T_p, while the D-band shifts towards lower wavenumbers from 1379 cm^{-1} for CN_x/400 to 1331 cm^{-1} for CN_x/800 and from 1356 to 1333 cm^{-1} for corresponding A/CN_x samples. The D-band shift is attributed to the transition of amorphous to graphitic ordered phase with increasing T_p, and is also supported by the XRD analysis, which reveals no crystalline order at lower T_p (T_p of 400 to 700 ^{o}C) with a marked increase for T_p of 800 ^{o}C. However, no significant changes in the bulk crystalline structures are observed for T_p of 400 to 700 ^{o}C from XRD while a gradual increment in graphitic order is observed by Raman spectroscopy. Again, with acid-treatment, larger shifts towards lower wavenumbers are observed for CN_x prepared at lower T_p as compared to those for higher T_p. For example, with acid-treatment, CN_x/400 exhibits a shift of 23 cm^{-1} in D-band, while the corresponding shift for T_p of 800 ^{o}C remains as low as 2 cm^{-1}. This is attributed to the removal of the disordered and acid-unstable phases from the CN_x synthesized at lower T_p during acid-treatment.
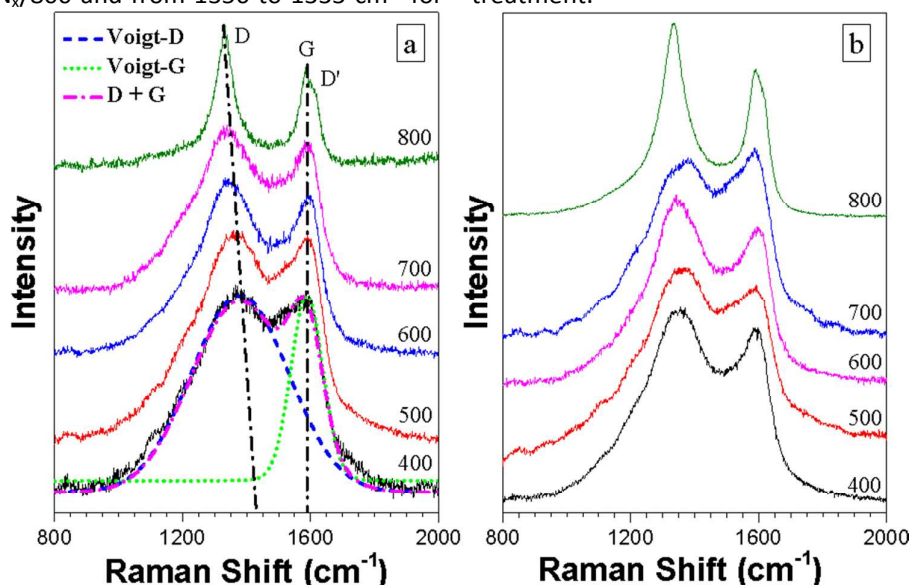

Fig. 3: Raman spectra of (a) CN_x and (b) A/CN_x electrocatalysts synthesized at different T_p values Typical Voigt fit for CN_x/400 along with individual D and G components is also shown (dotted curves).

The effects of T_p and the acid-treatment on X_N are demonstrated in Fig. 4a. With increasing T_p, X_N changes marginally for T_p of 400 to 700 ^{o}C as the carbonization of PVP completes below 450 ^{o}C and no major structural changes occur in between 500 to 700 ^{o}C. On the other hand, sharp decrease in X_N at T_p of 800 ^{o}C indicates significant structural changes in the CN_x leading to the graphitic arrangement. Again, the A/CN_x electrocatalysts exhibit increased X_N over their as-synthesized counterparts, which may be attributed to the removal of an N-deficient phase of carbon by acid-treatment.

To study the effects of T_p and acid-treatment on the structure of CN_x, the Raman spectra were further analyzed by fitting the data with Voigt distribution. While two peaks corresponding to the D and G bands are considered to fit the spectra for $T_p<800$ ^{o}C, the spectrum for T_p of 800 ^{o}C are fitted by using three components corresponding to the D, G and D' bands. Typical Voigt distribution fit for the Raman spectrum of CN_x/400, along with their D and G components, is shown in Fig. 3a. Among various parameters, full width at half maximum (FWHM) of D and G band (W_D and W_G) are taken as the parameters associated to α_D. Cuesta et al. have demonstrated that the W_D exhibits good correlation with α_D over a large range of order-disorder, while W_G correlates well with α_D for the carbons having high graphitic order.[43] As the CN_x

electrocatalysts of the present study have large range of disorder, ratio of D to G band FWHM (W_D/W_G) is considered as the measure of α_D. Fig. 4b shows the variations of W_D, W_G and W_D/W_G with T_p for the CN_x as well as A/CN_x electrocatalysts. The parameters W_D and W_D/W_G decrease marginally with increasing T_p from 400 to 700 °C, while for T_p of 800 °C, a noticeable decrement is observed. This, combined with the XRD analysis, suggests a significant structural difference between the CN_x synthesized at and below 800 °C. For both CN_x and A/CN_x, the W_G/W_D decreases with increasing T_p, exhibiting lowest value for CN_x/800, due to the decreased fraction of disordered phase. Furthermore, with acid-treatment, W_D/W_G decreases for T_p of 400 to 700 °C due to the removal of acid unstable disordered carbon, which leads to a decrease in W_D. On the other hand, due to the lower fraction of such acid-unstable disordered carbon in CN_x/800, W_D and thus, W_D/W_G increases with acid-treatment, which is due to the oxidation induced surface defects in the graphitic carbon.
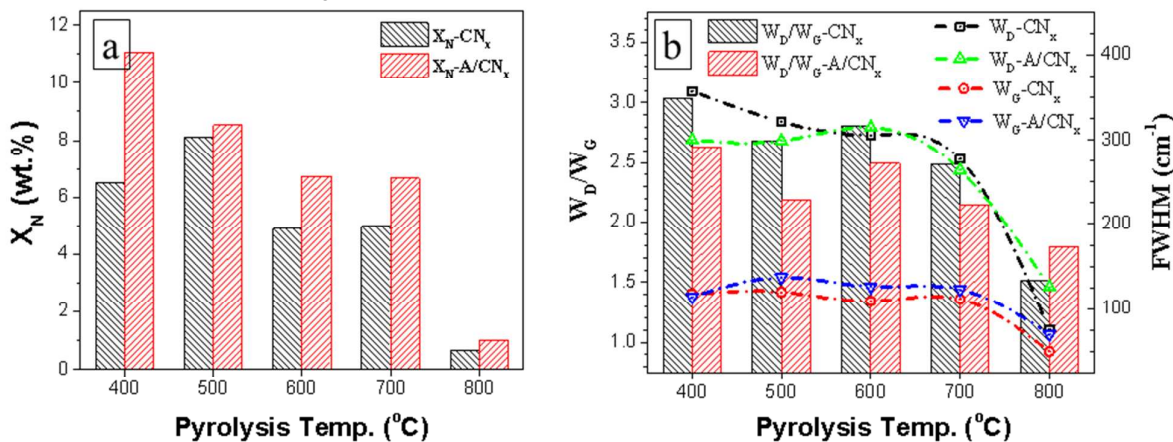

Fig. 4: Variations of structural parameters (a) X_N and (b) W_D/W_G, (W_D and W_G obtained from Raman spectra) with T_p for as-synthesized and acid-treated CN_x.

Since the Raman spectroscopy and XRD analysis suggest highest graphitic order for CN_x synthesized at T_p of 800 °C, surface morphologies of CN_x/800 and A/CN_x/800 were examined by SEM and AFM to evaluate the effect of acid-treatment on their surface structures (Fig. 5). Untreated CN_x consists of a layered structure covered with small particles (Fig. 5a), which are removed by acid-treatment (Fig. 5c). This reveals the presence of two phases, namely the acid-unstable amorphous phase and the crystalline layered phase in the CN_x. As the Raman spectroscopy suggests an increased graphitic order for A/CN_x/800, the particulate phase of CN_x/800 consists of amorphous carbon. Higher resolution image shown in the inset of Fig. 5a and the AFM image of Fig. 5b reveal rough morphology of the CN_x/800 surface. Inset of Fig. 5c exhibits higher resolution image of acid-treated CN_x, revealing the presence of pits (<100 nm; marked by arrows) on the surface. Similar pits can also be observed in the AFM image of Fig. 5d. On the other hand, no such pits are observed on the untreated CN_x surface. This may be attributed either to the pit formation by acid-induced oxidation or to the emergence of pre-existing pits by removal of amorphous carbon.[44] Embedded plots in Figs. 5a and 5c show the EDX spectra of corresponding samples revealing the effect of acid treatment on their elemental composition. Removal of leachable Co with acid-treatment is confirmed by reduction of the peak intensity.
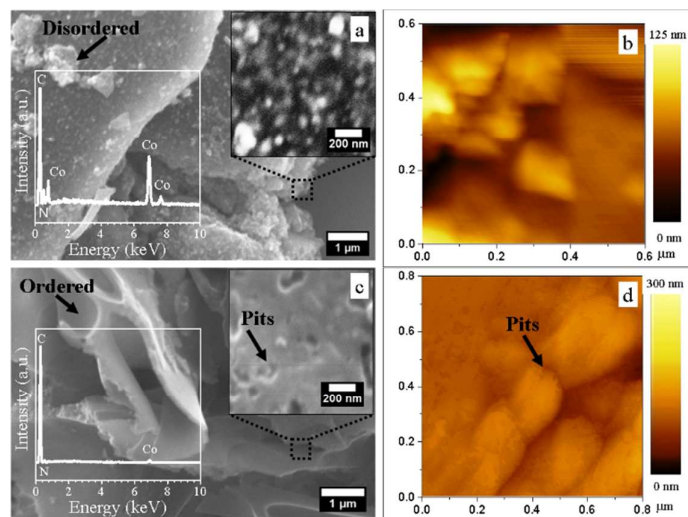
6 | *J. Mater. Chem. A.*, 2015, **00**, 1-16

This journal is © The Royal Society of Chemistry 20xx

Fig. 5: Surface morphology of untreated (a, b) and acid-treated (c, d) CN_x synthesized at T_p of 800 $^\circ$C as revealed by SEM (a, c) and AFM (b, d) imaging. Insets of (a) and (c) show the magnified views of the respective SEM images. Plots embedded in SEM images depict the EDX analysis of corresponding CN_x.

Chemical structures of the A/CN_x electrocatalysts synthesized at varying T_p are investigated using the FTIR spectroscopy as well as the XPS analysis. The FTIR spectra of A/CN_x shown in Fig. 6 exhibits strong absorption bands corresponding to (i) the OH stretching vibrations of surface hydroxyl groups and chemisorbed water at 3200–3600 cm^{-1}, (ii) various overlapped bands associated with N and/or O bound C between 1100 to 1700 cm^{-1}, and (iii) the weak absorption bands associated with the stretching vibrations of C-H bonds at ~2850 and ~2925 cm^{-1}.[45] The peak at ~1383 cm^{-1}, which exhibits highest intensities for T_p of 500 and 600 $^\circ$C, can be assigned to the strong absorption of NO_3^{-} . Similarly, the broad peak between 1300 to 1500 cm^{-1} consists of the in plane vibration of =C–H band at ~1330 cm^{-1},[46] the symmetric stretching of N=O at 1580 cm^{-1} and the stretching of the pyrrolic C-N bonds (1500 to 1590 cm^{-1}).[47] Again, the broad band at 1215 cm^{-1} observed for CN_x synthesized at higher T_p (700-800 $^\circ$C) may be associated to the coexisting C–O, C–O–C and O = C-O groups,[48] along with a contribution from the vibrations of the pyridine-type C-N bonds.[49] Furthermore, the peak around 1600 cm^{-1} may be assigned to the graphitic C=C at ~1650 cm^{-1},[47] C–C=O at ~1640 cm^{-1} [50] and C=N at ~1645 cm^{-1}.[51] Small peak at 1710 cm^{-1}, which remains well marked at lower T_p, is associated to the C = O stretching vibrations.[48] Hence, the FTIR spectra of the A/CN_x electrocatalysts reveal the presence of various groups consisting of N and/or O bound carbon, which could affect their catalytic activity.
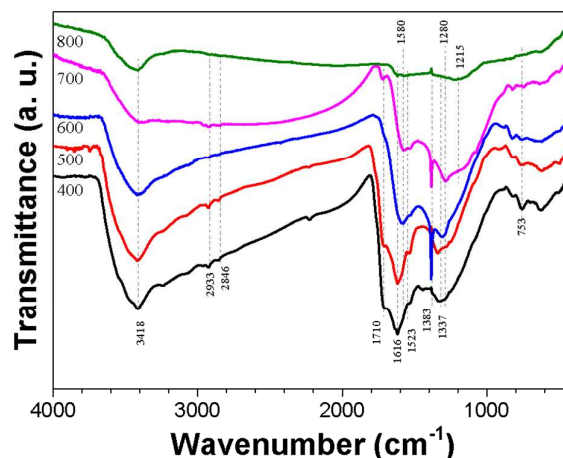

Fig. 6: FTIR spectra of A/CN_x synthesized at varying T_p.

Furthermore, to evaluate the effect of T_p on the surface elemental composition and chemical states of the constituent elements, XPS analysis of the selected A/CN_x samples was performed (Fig. 7). The XPS survey scans shown in the insets of Fig. 7a reveal the presence of N, O and Co, along with C in the A/CN_x electrocatalysts. The high-resolution XPS spectra corresponding to C 1s, N 1s, O 1s and Co 2p peaks analyzed by using XPSPEAK version 4.1 program are shown in Fig. 7, where Shirley-typed background and Gaussian–Lorentzian (GL) distributions are used to fit the baselines and the XPS peaks, respectively. Table 1 shows the surface elemental compositions of CN_x along with the distributions among various chemical states. The amounts of N, O and Co are represented in terms of the ratios X_N/X_C, X_O/X_C and X_{Co}/X_C, with X_C, X_O, and X_{Co}, being the at.% of C, O and Co, respectively. The distributions of the chemical states of constituent

elements vary significantly with T_p owing to the change in chemical states.

Table 1: Surface elemental compositions and chemical state distributions of A/CNx with varying T_p. The amounts of N, C and Co are shown in terms of ratios X_N/X_C, X_O/X_C and X_{Co}/X_C, which represent the fractional abundance of N, C and Co per unit of C.

T_p (°C) → Chemical states ↓	400	600	800
$X_C \times 100$ (at.%)	67.3	74.6	92.5
C=C sp^2 (at.%)	33.7	41.8	52.7
C–C sp^3/C=N sp^2 (at.%)	26.9	29.1	35.2
C–N sp^3 (at.%)	–	3.7	4.6
N–C=O (at.%)	6.7	–	–
$X_{Co}/X_C \times 100$	0.15	2.95	0.54
Co/Co$_x$O$_y$, Co–C–N	–	1.38	0.21
Co$_x$N$_y$–C, Co (NO$_3$)$_2$	–	1.57	0.33
CoO/Co$_3$O$_4$	0.15	–	–
$X_N/X_C \times 100$	9.21	11.53	0.76
Pyridinic-N	1.50	3.53	0.17
Pyrrolic/pyridine-N	4.85	4.64	0.35
Graphitic-N	1.72	1.78	2.5×10^{-2}
N-oxides	1.14	1.58	0.21
$X_O/X_C \times 100$	39.38	19.57	6.70
C–O–C	26.36	17.50	4.43
C=O	6.71	2.07	2.27
CoO/Co$_3$O$_4$	6.30	–	–

The components of C 1s peak at 284.4, 285.0, 286.7 and 287.7 eV (Fig. 7a) can be assigned to C–C (sp^2), C–C (sp^3)/C–N (sp^2), N–C=O and C–N (sp^3), respectively.[52-54] CN$_x$ synthesized at T_p of 400 °C contains the N-C=O chemical state of C, which disappears with increasing T_p. This is possibly due to the low temperature, which remains insufficient to break the PVP structure completely. Here, as revealed by the XRD analysis, the sp^2-hybridized C-C corresponds to the graphitic carbon for T_p of 800 °C while for 400 °C, it is possibly related to the partially decomposed PVP ring. Similarly, the N 1s peak consists of four components at 398.1, 399.8,

402.6 and 405 eV (Fig. 7b), which can be assigned to pyridinic N (N1), pyrrolic/pyridone N (N2), graphitic N (N3)[55, 56] and N-oxides such as NO$_3^-$ (N4), respectively.[57] The presence of N-oxides may be attributed to the formation of Co(NO$_3$)$_2$ from Co-oxides during HNO$_3$ treatment. Furthermore, as the N 1s peak from the Co bound N (Co$_x$N$_y$) has binding energy close to that of the pyridinic N, the peak at 398.1 eV contains both of these components.[58] The distribution of various chemical states of N exhibits highest fraction of pyridinic-N (the most ORR active component) for T_p of 600 °C. Again, at lower T_p, CN$_x$ electrocatalysts exhibit high O content, attributed to the presence of Co and/or N oxides and C bound O. The O 1s peak components at 531.2 and 533.0 eV (Fig. 7c) are associated with the C=O/NO$_3^-$ and C–O–C chemical states of O, respectively.[52, 55, 59] The peak at 533.0 eV may also contain a component corresponding to N–C=O chemical state of O. The extended XPS spectra of Co 2p shown in Fig. 7d reveal a clear evolution of the chemical state of cobalt from Co oxides (Co$_3$O$_4$ and CoO) at 400 °C to Co$_x$O$_y$, Co–C–N and Co$_x$N$_y$-C at 600 and 800 °C. For A/CN$_x$/400, the peaks at 777.5 and 778.4 eV are associated respectively to the spin 3/2 components of Co^{+2} and Co^{+3}, while the corresponding spin 1/2 components are observed at 792.8 and 793.9 eV.[60] The Co^{+2} and Co^{+3} components are attributed to the presence of Co-oxides. Hence, small amounts of Co-oxides remain present in A/CN$_x$-400, which are not detected by XRD. On the other hand, the A/CN$_x$ synthesized at higher temperatures exhibit no peaks corresponding to Co^{+2} and Co^{+3}, as can be seen in Fig. 7d. This is in agreement with the absence of diffraction peaks corresponding to Co-oxides in the XRD patterns. Hence, for T_p of 600 and 800 °C, the XPS peaks at 778.1, 780.0, 780.9, 782.6, eV can be assigned to Co/Co$_x$O$_y$ (Co1) Co–C–N (Co2), Co$_x$N$_y$–C (Co3), and Co (NO$_3$)$_2$ (Co4), respectively.[33, 34] Appearance of Co–C–N/Co$_x$N$_y$–C sites along with higher fractions of pyridinic-N and pyrrolic-N of CN$_x$ electrocatalysts synthesized at higher T_p could enhance their ORR activity significantly.
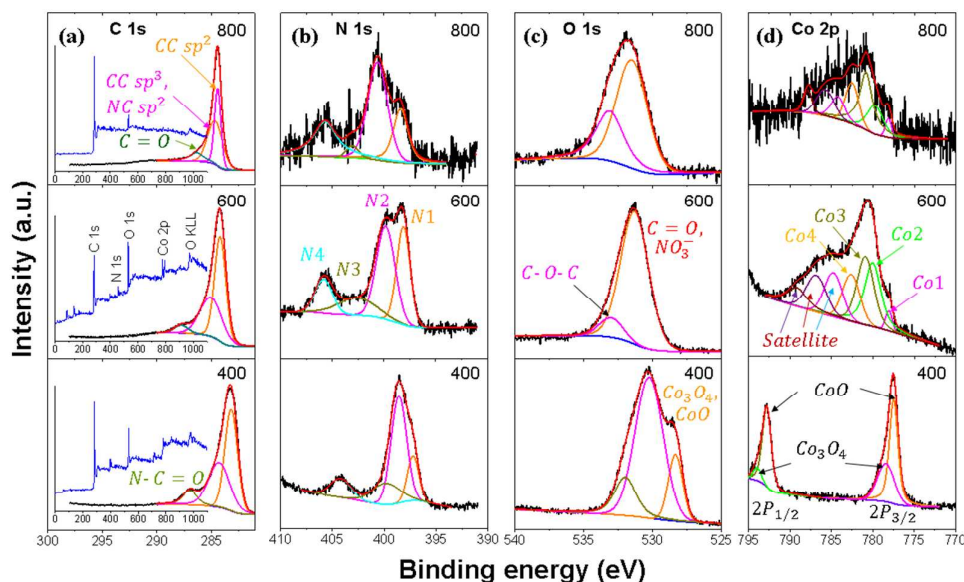
Fig. 7: XPS spectra of A/CN$_x$ synthesized at T$_p$ of 400, 600 and 800 ^{o}C exhibiting (a) C 1s, (b) N 1s, (c) O 1s and (d) Co 2p peaks fitted with various components by using Gaussian–Lorentzian (GL) distributions. XPS survey spectra corresponding to various T$_p$ are shown in the inset plots of (a).

Electrocatalytic performance

Cyclic voltammograms for CN$_x$ and A/CN$_x$ modified GC in O$_2$-saturated KOH (0.1 mol L^{-1}) are shown in Figs. 8a and 8b. The voltammograms exhibit a cathodic peak at a potential of ~ -0.4 V during reverse scan. On the other hand, CV curves in Ar-saturated electrolyte under similar conditions, shown in Figs. S1 and S2 (supplementary information), exhibit a pseudo-rectangular shape without redox peaks. This confirms the cathodic peak in O$_2$-saturated electrolyte to be originated from the ORR activity of the CNx electrocatalysts. With increasing T$_p$, the onset potential (V$_{Onset}$) for ORR shifts towards more positive potentials, exhibiting increased ORR performance.
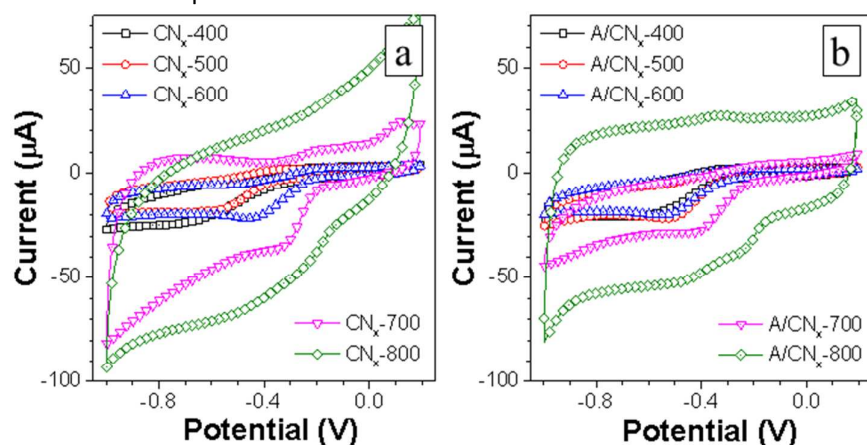

Fig. 8: Cyclic voltammograms of (a) as-synthesized and (b) acid-treated CN$_x$ in O$_2$ saturated aqueous 0.1 mol L^{-1} KOH at a scan rate of 50 mV/s.

The ORR activity of CN$_x$ electrocatalysts in alkaline media is further studied by LSV at a potential scan rate of 10 mV s^{-1} in O$_2$ saturated 0.1 mol L^{-1} KOH by using CN$_x$ modified GC RDE with a rotation rate of 1600 rpm. The LSV scans (capacitive current corrected) for the CN$_x$ and A/CN$_x$ modified RDE are shown respectively in Figs.

9a and 9b, while the corresponding Tafel plots (log(I) vs. potential) are presented in Figs. 9c and 9d. For comparison, LSV scan of Pt disc RDE (2 mm diameter),

recorded under similar conditions is also shown in Figs. 9a and 9b. The CN_x electrocatalysts show significant ORR activity, which increases with increasing T_p.
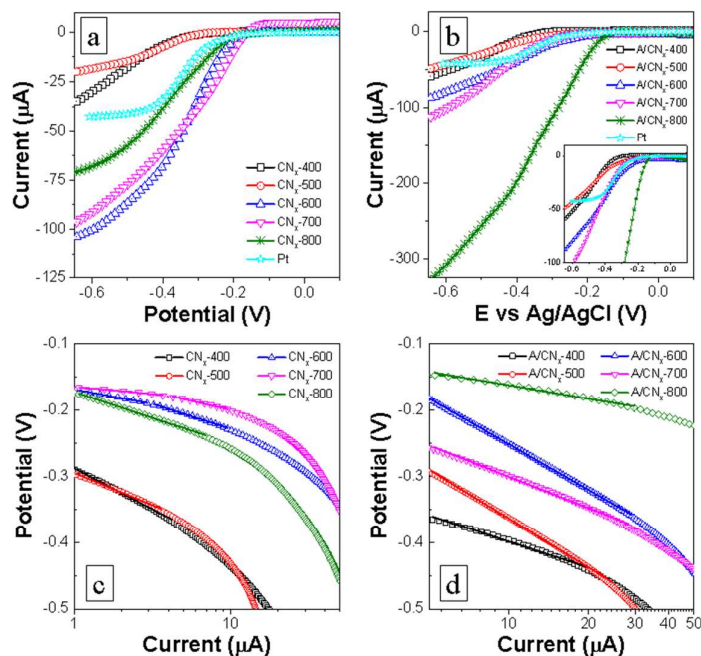

Fig. 9: (a, b) RDE voltammograms of the CN_x modified GC electrodes in 0.1 mol L^{-1} KOH at a scan rate of 10 mV s^{-1}. The voltammograms have been corrected for the capacitive current. (c, d) Tafel plots derived from (a and b).

To further evaluate the electrocatalytic performance of CN_x and A/CN_x, and to investigate the effects of temperature and acid-treatment on the ORR activity of CN_x electrocatalysts, the RDE voltammograms were analyzed further in terms of two different parameters, manely ORR peak height (I_{ORR}) and V_{Onset}, the ORR onset potential. The potential V_{Onset} is determined by drawing tangents at the points of slope change in the RDE voltammograms, while I_{ORR} at a particular potential (V= -0.4 V) is defined as the absolute difference between current values at V_{Onset} and V= -0.4 V. Physically, V_{Onset}, being the reaction overpotential–the minimum potential required to initiate the ORR, is related to the activity of the site. On the other hand, I_{ORR} can be associated with the density of catalytically active sites.[61] Since good electrocatalysts should provide an easy onset and a high current density, a less negative V_{Onset} (less overpotential) and high I_{ORR} may be considered as the desired characteristics for ORR catalysts. The variations of ORR parameters (I_{ORR} and V_{Onset}) for the CN_x electrocatalysts with T_p are shown in Table 2. Both the as-synthesized and acid-treated CN_x synthesized at or above 600 °C exhibit high ORR activity

in terms of V_{Onset} values comparable or superior to that for the Pt based catalysts (~ -210 mV).[36]

With increasing T_p, the V_{Onset} for both CN_x and A/CN_x shifts towards more positive potentials, suggesting the formation of highly ORR active sites. For example, with increasing T_p from 400 to 800 °C, values of V_{Onset} exhibit positive shifts of ~140 and ~210 mV for CN_x and A/CN_x electrocatalysts, respectively. Similarly, I_{ORR}, and thus the density of ORR active sites increases with T_p by respective factors of ~5 and ~18 for the CN_x and the A/CN_x electrocatalysts. The increase in ORR activity with T_p up to 700 °C may be attributed to the increased crystalline order, comparatively constant X_N, increasing number of ORR active C-N sites (pyridinic-N) and formation of Co–C–N/ Co_xN_y–C sites. Again, for T_p of 800 °C, despite sharp reduction in X_N, density of ORR active sites increases due to the increased graphitic nature, which increases the overall number of ORR active C-N, C-O-C and Co–C–N/ Co_xN_y–C sites.

Similar to T_p, acid-treatment of CN_x electrocatalysts also offers significant effect on their electrocatalytic performance, both in terms of I_{ORR} and V_{Onset}. With acid-treatment, ORR activity remains constant for T_p of 400 and 500 °C, decreases for T_p of 600 and 700 °C and

10 | *J. Mater. Chem. A*, 2015, **00**, 1-16

This journal is © The Royal Society of Chemistry 20xx

increases for T_p of 800 °C. The complex variation of I_{ORR} and V_{Onset} with acid-treatment for different CN_x samples could be associated with three factors, (i) the removal of disordered N-deficient phase of CN_x, effectively increasing X_N and I_{ORR}, (ii) the incorporation of oxygen containing groups with acid-treatment of the carbon surface[62], which can reduce I_{ORR} by steric hindrance and (iii) increased hydrophobicity of the acid-treated carbon, which could lead to increased adsorption of oxygen in small pores and thus increase the ORR activity. [63] While for lower T_p, the first factor dominates due to the presence of higher fraction of disordered carbon, at higher T_p, the density of active sites and hence I_{ORR} decreases due to the presence of oxide groups. The graphitized CN_x synthesized at 800 °C exhibits large increase in ORR activity with acid treatment due to increased crystalline order and X_N, combined with the modified surface morphology leading to increased hydrophobicity with acid treatment.

The large variation in Tafel slope with synthesis parameters is attributed to the changing chemical states of N, O and Co in the electrocatalysts. Particularly, lower Tafel slope for as-synthesized CN_x may be attributed to the presence of metallic Co and Co_3O_4 nanoparticles, which contribute to the ORR activity. The exceptionally high ORR activity of CN_x synthesized at T_p of 800 °C is attributed to the presence of graphitic carbon along with the pyridinic-N, as revealed by XRD, Raman and FTIR analysis.

Table 2: ORR parameters V_{Onset}, I_{ORR} and Tafel slope of the as-synthesized and the acid-treated CN_x obtained from the RDE voltammograms.

Parameters → T_p (°C) ↓	V_{Onset} (mV)		I_{ORR} at -0.4 V (µA)		Tafel slope (mV)	
	CN_x	A/CN_x	CN_x	A/CN_x	CN_x	A/CN_x
400	-356	-353	7	11	124	130
500	-310	-315	8	15	97	245
600	-211	-262	67	39	76	230
700	-152	-285	59	36	55	158
800	-215	-144	38	198	78	67

MOR activity

Cyclic voltammograms of CN_x modified GC electrodes in presence of CH_3OH (1.0 mol L^{-1} H_2SO_4 and 1.0 mol L^{-1} CH_3OH electrolyte, scan rate- 50 mV s^{-1}) reveal their

MOR activity. Typical CV scans for of the CN_x and A/CN_x electrocatalysts synthesized at T_p of 400 and 800 °C are shown in Fig. 10 (detailed; supplementary information, Fig. S3). For T_p of 400 °C, the electrocatalysts exhibit significant anodic current peaks at ~0.7 and ~0.6 V during forward and backward scans, which correspond respectively to the MOR and the oxidation of MOR byproducts on the electrode.[64, 65] However, in terms of the relative height of MOR peak, the MOR activity reduces significantly for T_p of 800 °C. The magnified views of the anodic peak corresponding to MOR are shown in the insets of Fig. 10, which suggest an enhancement in MOR activity with acid treatment for T_p of 400 °C, while a reduction for T_p of 800 °C. The MOR activity CN_x synthesized at low T_p could utilized in the catalyst layers of direct methanol fuel cells (DMFCs), where Pt supported on carbon is used as the MOR catalyst. MOR activity of the CN_x support may be employed to enhance the overall MOR activity of the Pt-based catalyst layer, which may ultimately reduce the required Pt-loading.
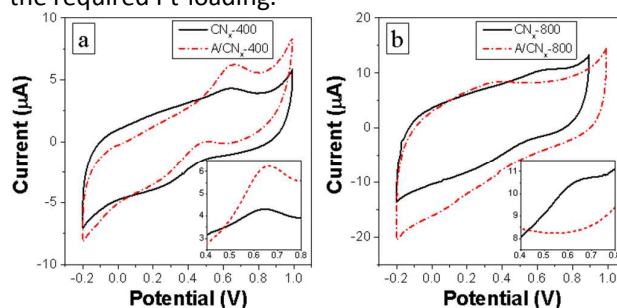

Fig. 10: Cyclic voltammograms in an electrolyte containing 1.0 mol L^{-1} H_2SO_4 and 1.0 mol L^{-1} CH_3OH at a scan rate of 50 mV s^{-1} for CN_x synthesized at T_p of (a) 400 and (b) 800 °C.

Correlation between electrochemical and structural parameters

Since the ORR parameters depend significantly on the two structural parameters, α_D and X_N of the CN_x, study of the correlations between these parameters for all the synthesized catalysts, irrespective of synthesis methods and sample modifications, is worthwhile. The variations of ORR parameters obtained from CV measurements, namely V_{Onset} (onset potential of ORR) V_{Peak} (potential at ORR current peak) and I_{ORR} ($|I_{V_{Peak}} - I_{V_{Onset}}|$, where, $I_{V_{Peak}}$ and $I_{V_{Onset}}$ are the current values at V_{Peak} and V_{Onset}, respectively) with structural parameters W_D/W_G and X_N for both the as-synthesized as well as the acid-treated CN_x are

provided in Fig. 11. Both V_{Onset}, and V_{Peak} exhibit linearly increasing trends with increasing W_D/W_G, suggesting poor electrocatalytic activities for highly disordered CN_x. Again, trends similar to those of the W_D/W_G variations are observed for the X_N variations of V_{Onset} and V_{Peak}. In contrast to the linear variations of V_{Onset} and V_{Peak}, with W_D/W_G, and X_N, the variations of I_{ORR} exhibit a more complex behavior. Accordingly, I_{ORR}

decreases linearly with increasing W_D/W_G or X_N for CN_x synthesized at T_p of 400 to 700 °C, while for T_p of 800 °C, it exhibits a sudden drop. At lower T_p, decrease in I_{ORR} with increasing W_D/W_G and X_N takes place as only a fraction of N (pyridinic-N) is ORR active. Thus, the combination having low α_D and high X_N proves to be most suitable for high electrocatalytic activity.
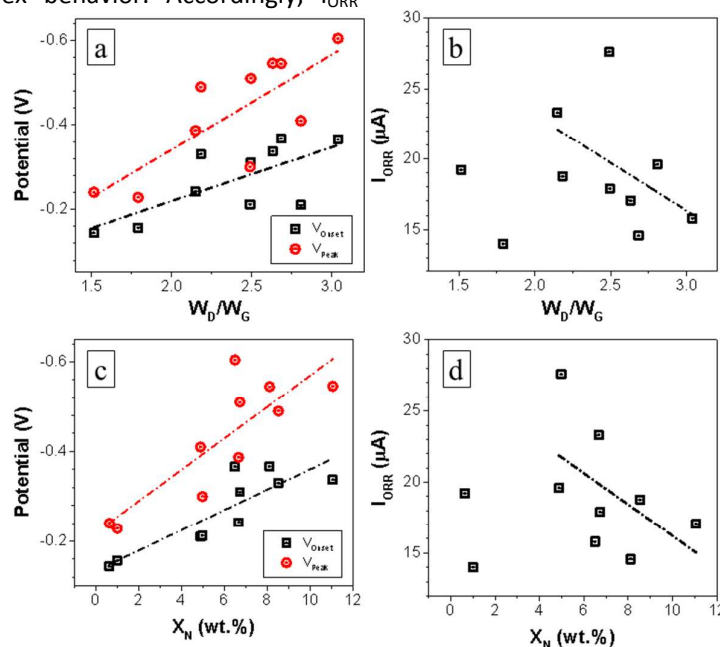

Fig. 11: Variations of CV parameters V_{Peak}, V_{Onset}, and I_{ORR} with W_D/W_G and X_N. The CV parameters of as-synthesized and acid-treated CN_x have been combined. The dashed lines show the trends.

To compare electrocatalytic performance of the present CN_x electrocatalysts with those previously reported, V_{Onset} obtained from CV curves is considered as the ORR activity parameter. Among numerous reports on carbon-based ORR electrocatalysts, only those articles having CV curves obtained in 0.1 mol L^{-1} KOH electrolyte at a scan rate of 50 mV/s were considered for comparisons. V_{Onset} for different catalysts were obtained by using a procedure similar to that adopted in the present study. To compare V_{Onset} calculated from CV plots that use a variety of reference electrodes, another comparable parameter $V_{Onset}(SHE) = V_{Onset} + V_{Ref}$, where V_{Ref} is the corresponding reference electrode potential with respect to standard hydrogen electrode (SHE), is defined. Fig. 12 summarizes the $V_{Onset}(SHE)$ for various catalyst systems including precious metals and other carbon-derived catalysts, which clearly suggests ORR activity of the present catalyst system to be

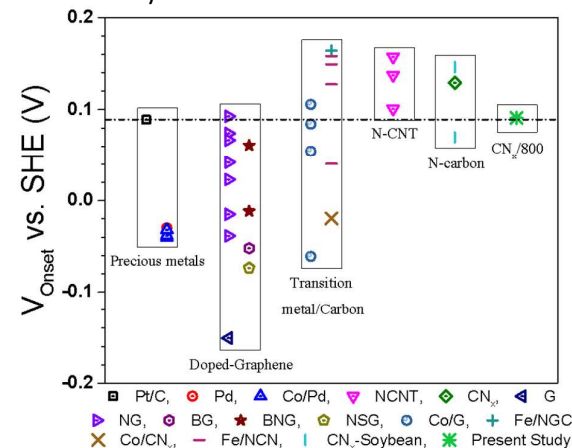comparable to those of Pt/C and other carbon-based electrocatalysts.

Fig. 12: Comparison of ORR electrocatalytic performance of the present electrocatalyst synthesized at T_p of 800 °C (CN_x/800, A/CN_x/800) with various catalyst systems such as- (i) precious metals and alloys (Pt,[8] Pd, Co/Pd[16]); (ii) N-doped CNT (N-CNT[6, 7]); (iii)

12 | *J. Mater. Chem. A*, 2015, **00**, 1-16

This journal is © The Royal Society of Chemistry 20xx

graphene (G) and doped G (N-doped G (NG), [8-13] boron-doped G (BG), [9] B-and N-codoped G (BNG) [9, 14] and S-and N-codoped G (SNG)[15]); (iv) transition metal containing carbon (Fe embedded N-graphitic carbon (Fe/NGC)[17], Fe–N/C nanofiber (Fe/NCN)[18], cobalt-graphene composite (Co/G),[19] cobalt containing N-carbon (Co/CN$_x$)[20]) and (v) N-carbon (CN$_x$) derived from pyrolysis of (a) ethylenediamine[2] and (b) soybean.[3]

Conclusions

In conclusion, N- and O- rich multi-doped carbon electrocatalysts, having ORR active pyridinic-N, pyrrolic-N and C- and N-bound O/Co sites, have been synthesized by low-temperature pyrolysis of a novel polymeric precursor and the effects of structural parameters on their ORR activity have been evaluated. While highly disordered N- and O-rich carbon is obtained at lower T_p (400 - 600 ^{o}C), graphitic carbon having lower N and O contents is obtained at 800 ^{o}C. Presence of ORR active C-N, C-O-C and Co–C–N/Co$_x$N$_y$–C sites makes the present multi-doped carbon materials highly active for ORR. Despite lower dopant concentrations, CN$_x$ synthesized at T_p of 800 ^{o}C exhibits highest ORR activity due to high graphitic order. Further, acid-treatment of CN$_x$ electrocatalysts can improve their ORR performance by the removal of ORR inactive disordered phase and the surface structure modifications. Moreover, the CN$_x$ synthesized at lower T_p exhibit MOR activity, which could be utilized to increase the effective performance of Pt-based catalyst layers for DMFCs by using the present catalysts as the catalyst layer support.

Acknowledgements

References

1. R. Jasinski, *Nature*, 1964, 201, 1212-1213.
2. X. Zhou, Z. Yang, H. Nie, Z. Yao, L. Zhang and S. Huang, *J. Power Sources*, 2011, 196, 9970-9974.
3. F. Liu, H. Peng, X. Qiao, Z. Fu, P. Huang and S. Liao, *Int. J. Hydrogen Energy*, 2014, 39, 10128-10134.
4. J. Xu, Y. Zhao, C. Shen and L. Guan, *ACS Appl. Mater. Interfaces*, 2013, 5, 12594-12601.
5. Z. Liu, H. Nie, Z. Yang, J. Zhang, Z. Jin, Y. Lu, Z. Xiao and S. Huang, *Nanoscale*, 2013, 5, 3283-3288.
6. K. Gong, F. Du, Z. Xia, M. Durstock and L. Dai, *Science*, 2009, 323, 760-764.
7. H. Li, H. Liu, Z. Jong, W. Qu, D. Geng, X. Sun and H. Wang, *Int. J. Hydrogen Energy*, 2011, 36, 2258-2265.

8. S. Ci, Y. Wu, J. Zou, L. Tang, S. Luo, J. Li and Z. Wen, *Chin. Sci. Bull.*, 2012, 57, 3065-3070.
9. Y. Xue, D. Yu, L. Dai, R. Wang, D. Li, A. Roy, F. Lu, H. Chen, Y. Liu and J. Qu, *Phys. Chem. Chem. Phys.*, 2013, 15, 12220-12226.
10. Z. Lin, G. H. Waller, Y. Liu, M. Liu and C.-p. Wong, *Nano Energy*, 2013, 2, 241-248.
11. Z. Lin, M.-k. Song, Y. Ding, Y. Liu, M. Liu and C.-p. Wong, *Phys. Chem. Chem. Phys.*, 2012, 14, 3381-3387.
12. L. Qu, Y. Liu, J.-B. Baek and L. Dai, *ACS Nano*, 2010, 4, 1321-1326.
13. D. Geng, Y. Chen, Y. Chen, Y. Li, R. Li, X. Sun, S. Ye and S. Knights, *Energy Environ. Sci.*, 2011, 4, 760-764.
14. S. Wang, L. Zhang, Z. Xia, A. Roy, D. W. Chang, J.-B. Baek and L. Dai, *Angew. Chem. Int. Ed.*, 2012, 51, 4209-4212.
15. Y. Su, Y. Zhang, X. Zhuang, S. Li, D. Wu, F. Zhang and X. Feng, *Carbon*, 2013, 62, 296-301.
16. S. Maheswari, S. Karthikeyan, P. Murugan, P. Sridhar and S. Pitchumani, *Phys. Chem. Chem. Phys.*, 2012, 14, 9683-9695.
17. A. Kong, X. Zhu, Z. Han, Y. Yu, Y. Zhang, B. Dong and Y. Shan, *ACS Catalysis*, 2014, 4, 1793-1800.
18. Y. Qiu, J. Yu, W. Wu, J. Yin and X. Bai, *J. Solid State Electrochem.*, 2013, 17, 565-573.
19. J. Wu, D. Zhang, Y. Wang, Y. Wan and B. Hou, *J. Power Sources*, 2012, 198, 122-126.
20. J. Qiao, L. Xu, L. Ding, P. Shi, L. Zhang, R. Baker and J. Zhang, *Int. J. Electrochem. Sci.*, 2013, 8, 1189-1208.
21. E. Gracia-Espino, F. López-Urías, H. Terrones and M. Terrones, *Mater. Express*, 2011, 1, 127-135.
22. P. H. Matter, E. Wang, M. Arias, E. J. Biddinger and U. S. Ozkan, *J. Mol. Catal. A: Chem.*, 2007, 264, 73-81.
23. Z. Chen, D. Higgins, H. Tao, R. S. Hsu and Z. Chen, *J. Phys. Chem. C*, 2009, 113, 21008-21013.
24. V. Stamenković, T. J. Schmidt, P. N. Ross and N. M. Marković, *J. Phys. Chem. B*, 2002, 106, 11970-11979.
25. P. H. Matter, L. Zhang and U. S. Ozkan, *J. Catal.*, 2006, 239, 83-96.
26. P. H. Matter, E. Wang and U. S. Ozkan, *J. Catal.*, 2006, 243, 395-403.
27. Y. Yang, J. Liu, Y. Han, H. Huang, N. Liu, Y. Liu and Z. Kang, *Phys. Chem. Chem. Phys.*, 2014, 16, 25350-25357.
28. R. Wang, T. Zhou, H. Li, H. Wang, H. Feng, J. Goh and S. Ji, *J. Power Sources*, 2014, 261, 238-244.
29. R. Silva, D. Voiry, M. Chhowalla and T. Asefa, *Journal of the American Chemical Society*, 2013, 135, 7823-7826.
30. G. Wu, Z. Chen, K. Artyushkova, F. H. Garzon and P. Zelenay, *ECS Trans.*, 2008, 16, 159-170.
31. H. Y. Qin, Z. X. Liu, W. X. Yin, J. K. Zhu and Z. P. Li, *J. Power Sources*, 2008, 185, 909-912.
32. T. Iwazaki, H. Yang, R. Obinata, W. Sugimoto and Y. Takasu, *J. Power Sources*, 2010, 195, 5840-5847.
33. M. Li, X. Bo, Y. Zhang, C. Han, A. Nsabimana and L. Guo, *J. Mater. Chem. A*, 2014, 2, 11672-11682.
34. A. Morozan, P. Jegou, B. Jousselme and S. Palacin, *Phys. Chem. Chem. Phys.*, 2011, 13, 21600-21607.
35. J. Liu, Y. Liu, N. Liu, Y. Han, X. Zhang, H. Huang, Y. Lifshitz, S.-T. Lee, J. Zhong and Z. Kang, *Science*, 2015, 347, 970-974.
36. R. Sharma and K. K. Kar, *Electrochim. Acta*, 2015, 156, 199-206.
37. Z.-H. Sheng, L. Shao, J.-J. Chen, W.-J. Bao, F.-B. Wang and X.-H. Xia, *ACS Nano*, 2011, 5, 4350-4358.

38. M. Cabo, E. Pellicer, E. Rossinyol, M. Estrader, A. Lopez-Ortega, J. Nogues, O. Castell, S. Surinach and M. D. Baro, *J. Mater. Chem.*, 2010, 20, 7021-7028.
39. H. Li and S. Liao, *J. Phys. D: Appl. Phys.*, 2008, 41, 065004.
40. F. J. Maldonado-Hódar, C. Moreno-Castilla, J. Rivera-Utrilla, Y. Hanzawa and Y. Yamada, *Langmuir*, 2000, 16, 4367-4373.
41. T. Gruber, T. W. Zerda and M. Gerspacher, *Carbon*, 1994, 32, 1377-1382.
42. A. Jorio, M. M. Lucchese, F. Stavale, E. H. M. Ferreira, M. V. Moutinho, R. B. Capaz and C. A. Achete, *J. Phys.: Condens. Matter*, 2010, 22, 334204.
43. A. Cuesta, P. Dhamelincourt, J. Laureyns, A. Martínez-Alonso and J. M. D. Tascón, *Carbon*, 1994, 32, 1523-1532.
44. H. Hu, B. Zhao, M. E. Itkis and R. C. Haddon, *J. Phys. Chem. B*, 2003, 107, 13838-13842.
45. W. Li, X.-Z. Tang, H.-B. Zhang, Z.-G. Jiang, Z.-Z. Yu, X.-S. Du and Y.-W. Mai, *Carbon*, 2011, 49, 4724-4730.
46. J. Zhu, X. Zhao, M. Xiao, L. Liang, C. Liu, J. Liao and W. Xing, *Carbon*, 2014, 72, 114-124.
47. H.-g. Wang, Y. Wang, Y. Li, Y. Wan and Q. Duan, *Carbon*, 2015, 82, 116-123.
48. I.-Y. Jeon, Y.-R. Shin, G.-J. Sohn, H.-J. Choi, S.-Y. Bae, J. Mahmood, S.-M. Jung, J.-M. Seo, M.-J. Kim, D. Wook Chang, L. Dai and J.-B. Baek, *Proc. Natl. Acad. Sci.*, 2012, 109, 5588-5593.
49. H. Peng, Z. Mo, S. Liao, H. Liang, L. Yang, F. Luo, H. Song, Y. Zhong and B. Zhang, *Sci. Rep.*, 2013, 3.
50. Y. Han and Y. Lu, *Carbon*, 2007, 45, 2394-2399.
51. Y. Mao, H. Duan, B. Xu, L. Zhang, Y. Hu, C. Zhao, Z. Wang, L. Chen and Y. Yang, *Energy Environ. Sci.*, 2012, 5, 7950-7955.
52. Z. Yang, M. Xu, M. Liu, F. He, F. Gao, Y. Su, H. Wei and Y. Zhang, *Nanoscale*, 2014, 6, 1890-1895.
53. T. Hu, X. Sun, H. Sun, G. Xin, D. Shao, C. Liu and J. Lian, *Phys. Chem. Chem. Phys.*, 2014, 16, 1060-1066.
54. H. Kim, I.-S. Bae, S.-J. Cho, J.-H. Boo, B.-C. Lee, J. Heo, I. Chung and B. Hong, *Nanoscale Res Lett*, 2012, 7, 1-7.
55. D. Hulicova-Jurcakova, M. Seredych, G. Q. Lu and T. J. Bandosz, *Adv. Funct. Mater.*, 2009, 19, 438-447.
56. K. Artyushkova, B. Kiefer, B. Halevi, A. Knop-Gericke, R. Schlogl and P. Atanassov, *Chem. Commun. (Cambridge, U. K.)*, 2013, 49, 2539-2541.
57. G. Yang, H. Hu, Y. Zhou, Y. Hu, H. Huang, F. Nie and W. Shi, *Sci. Rep.*, 2012, 2.
58. G. Wu, C. M. Johnston, N. H. Mack, K. Artyushkova, M. Ferrandon, M. Nelson, J. S. Lezama-Pacheco, S. D. Conradson, K. L. More, D. J. Myers and P. Zelenay, *J. Mater. Chem.*, 2011, 21, 11392-11405.
59. G. Ma, R. Jia, J. Zhao, Z. Wang, C. Song, S. Jia and Z. Zhu, *J. Phys. Chem. C*, 2011, 115, 25148-25154.
60. R. Ding, L. Qi, M. Jia and H. Wang, *Nanoscale*, 2014, 6, 1369-1376.
61. J.-P. Dodelet, in *Electrocatalysis in Fuel Cells*, ed. M. Shao, Springer London, 2013, vol. 9, ch. 10, pp. 271-338.
62. J. S. Noh and J. A. Schwarz, *Carbon*, 1990, 28, 675-682.
63. C. O. Ania, M. Seredych, E. Rodriguez-Castellon and T. J. Bandosz, *Appl. Catal., B*, 2015, 163, 424-435.
64. C.-H. Wang, H.-C. Shih, Y.-T. Tsai, H.-Y. Du, L.-C. Chen and K.-H. Chen, *Electrochim. Acta*, 2006, 52, 1612-1617.
65. L. Zhang, J.-J. Shao, W. Zhang, C. Zhang, X. Zheng, H. Du and Q.-H. Yang, *J. Phys. Chem. C*, 2014, 118, 25918-25923.

14 | *J. Mater. Chem. A.*, 2015, **00**, 1-16

This journal is © The Royal Society of Chemistry 20xx

Graphical and textual abstract

Effects of pyrolysis temperature and acid-treatment on oxygen reduction catalytic activity of N-, O- and Co-doped carbons have been studied.